


PAPER

[View Article Online](#)
[View Journal](#)


Cite this: DOI: 10.1039/d5nr01935d

Mg-doped layered vanadates for high-energy zinc anode-based electrochromic devices†

 Haoyang Dong,^a Mengjie Zhu,^a Caofeng Niu,^a Guolong Zhou,^a Tongzhuang He,^a Bing Xu^{*a} and Jingwei Chen  ^{*a,b}

Zinc anode-based electrochromic devices (ZECDs) demonstrate promising prospects in dual-functional electrochromic (EC)–energy storage systems due to their unique optical and energy retrieval properties. Vanadates are widely used in ZECDs due to their diverse color properties, but their cycling stability and kinetics are often hindered by the strong electrostatic interactions between Zn^{2+} ions and the host vanadate lattice. In this study, we fabricated magnesium ion-doped layered vanadates (MVO) with effectively enlarged interlayer spacing, promoting rapid insertion/extraction of Zn^{2+} . Compared to undoped ammonium vanadate (VO), the MVO electrode exhibits superior electrochemical capacity (57.6 mAh m^{-2}), faster switching kinetics ($t_c = 79.6 \text{ s}$, $t_b = 25.2 \text{ s}$), enhanced coloration efficiency, and excellent electrochemical reversibility. Finally, the fabricated ZECDs employing MVO films demonstrate exceptional electrochemical reversibility, promising optical switching performance and excellent cycling stability (500 cycles). These results validate the effectiveness of the Mg-doping strategy for the modification of layered vanadates for optimized ZECDs coupling EC and energy storage functionalities.

 Received 12th May 2025,
 Accepted 18th June 2025

DOI: 10.1039/d5nr01935d

rsc.li/nanoscale

Introduction

Overreliance on fossil fuels has exacerbated global environmental pollution, driving the urgent demand for energy-efficient and eco-friendly energy systems.^{1–3} As one of the most prevalent energy storage technologies, batteries have garnered significant attention due to their inherent advantages in performance and portability, aligning with the requirements of sustainability.⁴ Additionally, efficient integration of batteries with other technologies can cater multifunctional applications. In particular, coupling batteries with electrochromic (EC) technology has become an emerging and greatly prospective research direction.⁵ The structural and mechanistic similarities between electrochromic devices (ECDs) and batteries make their integration feasible and highly intriguing.^{6–11} Electrochromism refers to the phenomenon where materials undergo reversible optical property changes (e.g., transmittance, absorption, and reflectance) due to redox reactions under alternating voltages,^{12–14} finding applications in smart windows, displays, and satellite thermal control.^{15–17} However, conventional intercalation-based ECDs face limitations due to the strong corrosiveness of H^+ , high cost of Li^+ , and large ionic radius of Na^+ , leading to suboptimal redox kinetics and poor optical/electrochemical performance.^{16,18–21} Recent exploration of multivalent ions has highlighted Zn^{2+} as a promising candidate due to its low redox potential (-0.76 V vs. standard hydrogen electrode), high theoretical capacity (820 mAh g^{-1}), cost-effectiveness, and stability in aqueous electrolytes.

^aSchool of Materials Science and Engineering, Ocean University of China, Qingdao 266100, China. E-mail: bxu0117@163.com, chenjingwei@ouc.edu.cn

^bQingdao Key Laboratory of Marine Extreme Environment Materials, Qingdao 266404, China. E-mail: chenjingwei@ouc.edu.cn

† Electronic supplementary information (ESI) available. See DOI: <https://doi.org/10.1039/d5nr01935d>



Jingwei Chen

Jingwei Chen obtained his Ph.D. in 2019 from Nanyang Technological University (NTU), under the supervision of Prof. Lee Pooi See. He worked as a research fellow in NTU from 2019 to 2021, and joined School of Materials Science and Engineering, Ocean University of China as an associate professor in 2021. His research interests include electrode/electrolyte interfacial engineering for advanced energy storage and

conversion devices, e.g. electrochemical metal ion battery and electrochromic devices.

Rechargeable aqueous zinc-ion batteries (ZIBs) and Zn-anode based electrochromic devices (ZECs) have thus become research hotspots.^{5,16,22–25}

Vanadium-based materials are widely employed as ZIB and ZEC cathodes owing to their low cost, abundant reserves, high theoretical capacity ($\sim 400 \text{ mAh g}^{-1}$), and open-layered frameworks, facilitating rapid and reversible Zn^{2+} intercalation/deintercalation. Among these, V_2O_5 is also a typical inorganic multi-color EC material, yet its application in ZECs is still hindered by the strong electrostatic interaction between Zn^{2+} and the V_2O_5 lattice, leading to poor reversibility, poor cycling stability, slow kinetics, and dissolution into aqueous electrolytes.^{14,23,24,26–29} In general, the performance of ZECs, such as switching time and coloration efficiency (CE), is related to the radius of the inserted ions and their diffusion kinetics in the host material.^{30,31} Approaches such as defect engineering, nano-structuring and ion doping have been reported to improve the electrochemical performance of V_2O_5 . For example, introducing defects into V_2O_5 offers more Zn^{2+} active sites and enhances kinetics and cycling performance.^{14,32–35} Alternatively, Liu *et al.* significantly improved the cycling stability, rate performance and electrochemical capacity of V_2O_5 by inducing the vertical growth of $\text{V}_2\text{O}_5 \cdot n\text{H}_2\text{O}$ nano-arrays on VS_x microbars.³⁶ In addition, cation doping can improve the cycling stability, rate performance and capacity of vanadium-based compounds by expanding the interlayer spacing and weakening the strong electrostatic interaction between Zn^{2+} and the layer structure, while alleviating the bulk strain in electrodes. To date, various cations including Li^+ , Na^+ , K^+ , Ca^{2+} , and Zn^{2+} have been investigated for this purpose.^{28,37–42} However, interlayer spacing expansion brought about by monovalent cations is often limited. For example, with interlayer spacing expansion from 0.79 nm to 0.87 nm, about 10%,^{43,44} sodium vanadate (SVO) exhibited capacity retention of only 14.78% after 500 cycles, at a non-ideal switching speed.^{45,46}

The extent of V_2O_5 interlayer expansion is intrinsically correlated with both the ionic radius and charge density of the incorporated metal cations.^{47,48} While divalent Zn^{2+} and Ca^{2+} possess relatively large ionic radii, their intercalation may induce lattice distortion in the V_2O_5 framework.⁵ In contrast, Mg^{2+} exhibits a relatively smaller ionic radius, lower molecular weight, and significantly higher charge density ($3.08 \text{ e } \text{\AA}^{-3}$), enabling Mg^{2+} to effectively polarize the interlayer O^{2-} species in V_2O_5 , thereby weakening the interlayer van der Waals forces and substantially expanding the interlamellar spacing.^{48–50} Consequently, Mg^{2+} -doped vanadates demonstrate improved electrochemical performance,^{42,51} and are envisioned to offer superior EC properties.

In this work, Mg^{2+} doped V_2O_5 (MVO) was synthesized *via* a hydrothermal method, showing enlarged interlayer spacing by $\Delta d = 0.09 \text{ nm}$ (from 0.21 nm to 0.30 nm, about 40%). The MVO colloidal solution was blade-coated onto F-doped SnO_2 (FTO) glass and annealed to form an EC electrode, exhibiting a high electrochemical capacity of 57.6 mAh m^{-2} at 0.01 mA cm^{-2} , excellent cycling stability (500 cycles) and improved rate

capability. Additionally, the MVO electrode demonstrated faster switching speeds ($t_c = 79.6 \text{ s}$, $t_b = 25.2 \text{ s}$), higher CE, and superior optical performance compared to undoped VO, highlighting its potential for ZEC applications.

Experimental section

Synthesis of magnesium vanadate (MVO)

All reagents were analytical grade and used without further purification. NH_4VO_3 (3.6 mM) was dissolved in 144 mL de-ionized water under heating (80 °C) and stirring. After cooling to room temperature, the solution pH was adjusted to ~ 3 using 2 M HCl. $\text{MgCl}_2 \cdot 6\text{H}_2\text{O}$ (7.2 mM) was then added under vigorous stirring. After 15 min, the solution was transferred equally into two 100 mL Teflon-lined autoclaves and heated at 160 °C for 6 h. The precipitate was washed three times with de-ionized water and twice with ethanol, followed by freeze-drying for 24 h. The dried product was ground to obtain MVO powder. VO (undoped vanadate) was synthesized following the same procedures described above, except that no $\text{MgCl}_2 \cdot 6\text{H}_2\text{O}$ was added.

Fabrication of the MVO electrochromic film

Hydroxyethyl cellulose (HEC, $M_w \approx 30\,000$) and FTO-coated glass were purchased from Sinopharm Chemical Reagent Co., Ltd and Wuhan Jingge Solar Technology Co., Ltd, respectively. A colloidal suspension was prepared by dispersing MVO in de-ionized water (8 mg mL^{-1} , 5 mL). HEC (0.1 g) was added, and the mixture was stirred at 60 °C for 24 h to form a viscous precursor. The precursor was blade-coated onto FTO glass and annealed at 200 °C for 24 h in a muffle furnace. The resulting MVO/FTO film was cooled to room temperature for further use.

Characterization

The microstructures of the EC electrodes were characterized using scanning electron microscopy (Gemini SEM 300) and transmission electron microscopy (TEM, JEOL 2010F). The phase composition and surface chemical states of the samples were analyzed *via* powder X-ray diffraction (XRD, Bruker D8) and X-ray photoelectron spectroscopy (XPS, Thermo Scientific K-Alpha). The Raman spectrum of MVO powder was collected using a laser Raman spectrometer (HORIBA LabRAM HR800, laser excitation: 532 nm). All electrochemical tests were performed on an electrochemical workstation (CHI760E, Shanghai Chenhua Instruments, Inc.) using a conventional two-electrode system, where Zn foil served as the counter electrode, 0.5 M ZnSO_4 acted as the electrolyte, and the prepared MVO/FTO (active area $1.2 \times 0.8 \text{ cm}^2$) functioned as the working electrode. The optical properties and switching time of the MVO EC film (active area $5 \times 0.8 \text{ cm}^2$) were investigated using a UV-vis spectrophotometer (UV-2600i, Shimadzu). The electrochemical and EC performance of the ZEC was evaluated by employing MVO/FTO as the cathode, Zn foil as the anode, and 0.5 M ZnSO_4 as the electrolyte.

Results and discussion

Morphology and physical characterization

The detailed preparation process of MVO electrodes is schematically depicted in Fig. 1. Initially, nano-sized MVO was synthesized *via* a hydrothermal method. Subsequently, the MVO colloid was evenly scrape-coated on FTO glass. MVO electrodes were then obtained after heating and annealing at 200 °C in a muffle furnace. Without Mg-doping, VO consists of nanosheets with dimensions of 3–5 μm stacked together, forming a lamellar structure (Fig. S1†). Nonetheless, MVO consists of nanoparticles of varying sizes from 100 to 300 nm, with a layered structure similar to that of VO (Fig. S2a and Fig. S1b†). The cross-sectional SEM image of the MVO electrode was also col-

lected (Fig. S2b†), demonstrating a uniform MVO coating with a thickness of approximately 1 μm on the FTO substrate. The crystal structure and elemental distribution of MVO and VO were further investigated with TEM (Fig. 2a–c, Fig. S1c, d†). Lamellar MVO consists of finer nanosheets (about tens of nanometers), and the lattice fringes of 0.30 nm are indexed to the (001) crystallographic plane of MVO, markedly expanded compared to the 0.21 nm spacing observed in VO (Fig. S1c†). Energy dispersive X-ray spectroscopy (EDS) maps (Fig. 2c and Fig. S1d†) confirm the successful synthesis of MVO and VO, and the uniform distribution of Mg proves that Mg^{2+} is uniformly doped into the V_2O_5 lattice.⁵² The diffraction patterns present in selected area electron diffraction (SAED) observations (Fig. 2b) further proved the higher crystallinity of MVO than that of VO (Fig. S1c†). These results collectively validate the successful intercalation of Mg^{2+} into the V_2O_5 interlayers while preserving the original morphological integrity.

The crystal composition of MVO was characterized by powder X-ray diffraction (XRD) analysis. All diffraction peaks of MVO exhibit exact correspondence with the reference pattern of the $\text{Mg}_2\text{V}_6\text{O}_{17}$ phase (JCPDF#28-0643), thus confirming the phase purity and successful synthesis of MVO (Fig. 3a). In contrast, the diffraction pattern of VO is indexed to ammonium vanadate (JCPDF#22-1046). A comparison of the two XRD patterns (Fig. 3a) reveals that the (001) diffraction peak of MVO exhibits broadening along with a slight shift

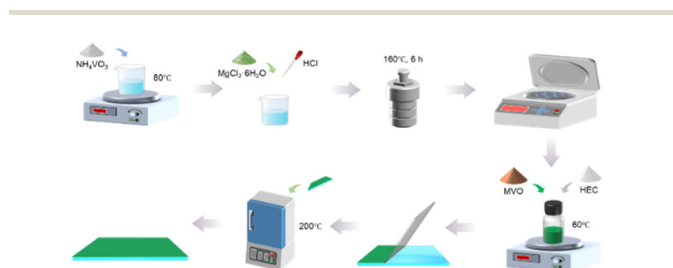


Fig. 1 Schematic illustration of the preparation process of the MVO electrode.

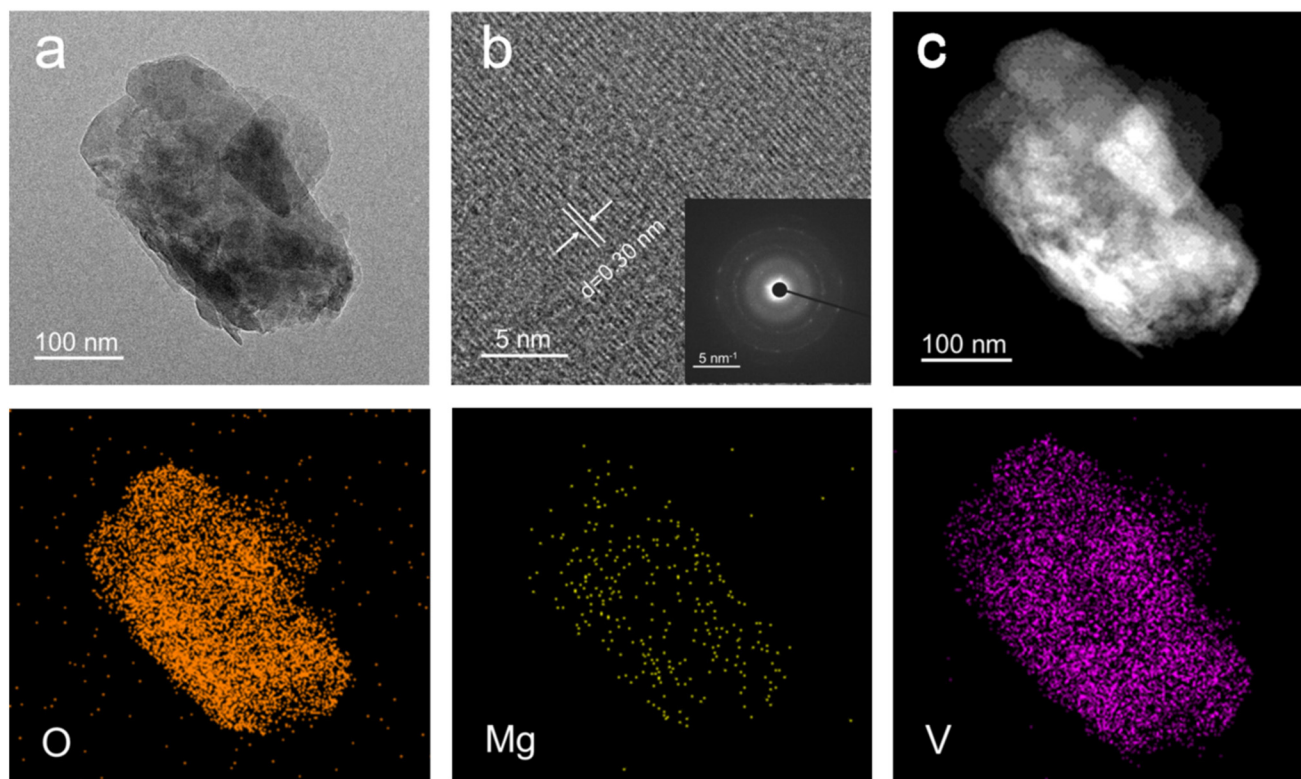


Fig. 2 Electron microscope observations of MVO. (a) TEM image of MVO. (b) High-resolution TEM (HRTEM) image of MVO. (c) HAADF-STEM image of MVO and the corresponding elemental maps.

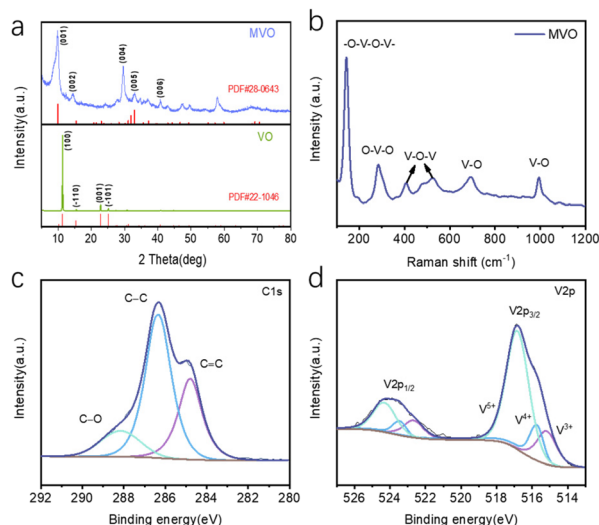


Fig. 3 Crystal and chemical structure characterization of MVO. (a) XRD patterns of MVO and VO. (b) Raman spectrum of MVO. High resolution (c) C 1s and (d) V 2p XPS spectra of MVO.

toward lower angles, confirming a significant expansion of the interlayer spacing in the host lattice due to the insertion of Mg^{2+} ions.^{47,53} Fig. 3b presents the Raman spectrum of MVO, highlighting its characteristic bands and elucidating the vibration modes. Specifically, the spectrum reveals the -O-V-O-V- bond at 140 cm^{-1} , the O-V-O bond at 282 cm^{-1} , the V-O-V bonds at 404 cm^{-1} and 525 cm^{-1} , and the V=O bonds at 693 cm^{-1} and 993 cm^{-1} .⁵⁴ *Ex situ* XPS analysis was also performed on MVO films to investigate their chemical composition and bonding states. The XPS survey spectrum of MVO nanofilms (Fig. S3†) confirms the presence of characteristic peaks corresponding to C 1s, V 2p, and O 1s. High-resolution spectra of C 1s, V 2p and O 1s were subjected to peak deconvolution using Gaussian-Lorentzian functions. As shown in Fig. 3c, d and Fig. S4,† the C 1s spectrum was deconvoluted into three distinct components at 284.8 eV, 286.5 eV, and 288.6 eV, which are attributed to the C=C, C-C, and C-O bonding configurations, respectively. Three pairs of characteristic peaks were identified in V 2p_{3/2} and V 2p_{1/2}, located at 524.5 eV and 517 eV, 523.6 eV and 515.9 eV, and 522.8 eV and 515.2 eV, corresponding to the characteristic peaks of V^{5+} , V^{4+} and V^{3+} respectively. The larger areas of V^{5+} peaks also indicate the dominant V^{5+} valence state in MVO. After the deconvolution of the O 1s spectrum, the signals at 529.6 eV, 532.0 eV, and 532.8 eV were, respectively, attributed to the different forms of O^{2-} associated with V-O, O-H, and H_2O .⁵⁰

Evaluation of electrochemical and electrochromic performance

The EC properties of MVO were investigated using a two-electrode configuration with zinc foil as the counter electrode and 0.5 M ZnSO_4 aqueous electrolyte. First, the galvanostatic charge-discharge (GCD) curves of VO and MVO at various current densities were analyzed to quantify the specific

capacities (Fig. S5†). The obviously longer discharging times of MVO than those of VO under identical current densities clearly indicate the enhanced specific capacity and superior energy storage capability of MVO. The areal capacity can be thus derived from GCD measurements (Fig. 4a), offering capacities of 57.6, 48.6, 23.7, 12.8, and 7.4 mAh m^{-2} for MVO electrodes at current densities of 0.01, 0.02, 0.05, 0.1, and 0.2 mA cm^{-2} , respectively. Notably, MVO demonstrates superior rate performance to VO (Fig. S6 and S7†). Cyclic voltammetry (CV) measurements within 0.2–2 V (Fig. 4b) reveal well-defined redox peaks with increased peak current responses to scan rate variations, demonstrating the superior electrochemical reversibility of MVO. The larger CV integral areas and enhanced peak currents with reduced polarization observed in MVO, compared to VO (Fig. S8†), confirm its improved capacity and reaction kinetics. The enhanced electrochemical performance is attributed to the effective Mg^{2+} doping that enlarges the layer spacing of the V_2O_5 lattice, while the fine nanosheets provide larger surface area and more active sites for Zn^{2+} embedding. The GCD profiles and CV analyses collectively validate the exceptional electrochemical performance of MVO, resulting in enhanced redox kinetics and rate performance owing to the effective Mg^{2+} pillars that provide expanded interlayer spacing.

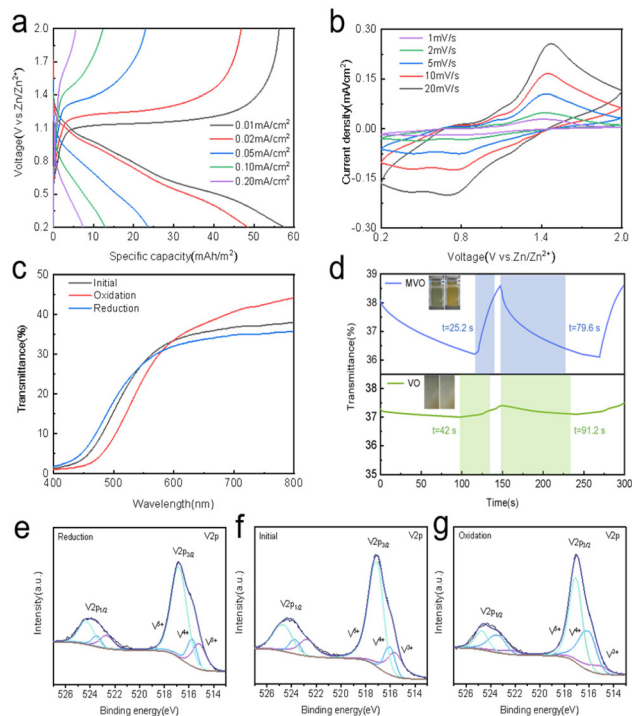


Fig. 4 The electrochemical and EC properties of MVO. (a) GCD curves of MVO at different current densities. (b) CV curves of MVO at different scanning rates. (c) Transmission spectra of the initial, reduced and oxidized states of MVO at 400–800 nm. (d) *In situ* transmittance response of MVO and VO at 650 nm at voltage steps of 0.2 V for 120 s and 2 V for 30 s and digital photographs in colored and bleached states. High-resolution XPS spectra of V 2p in MVO in the (e) reduced state, (f) initial state, and (g) oxidized state.

Subsequently, the EC properties of MVO were also investigated using a two-electrode configuration with a zinc foil counter electrode and 0.5 M ZnSO_4 aqueous electrolyte. Ultraviolet-visible (UV-vis) transmittance spectra (Fig. 4c) were recorded across 400–800 nm for the initial, reduced (0.2 V, 120 s), and oxidized (2 V, 120 s) states, showing transmittance changes at different wavelengths due to the color change in MVO. To more clearly demonstrate the color variation, we constructed a CIE1931 chromaticity chart (Fig. S9†) to quantify and distinguish the different optical states of MVO. In contrast, VO shows minimal transmittance variations in both the oxidized and reduced states (Fig. S10†), revealing the inferior EC performance in VO. Notably, MVO shows wavelength-dependent transmittance modulation, normally originating from altered light absorption characteristics caused by valence state variations of vanadium during Zn^{2+} intercalation/deintercalation in the EC process.⁵⁵ In addition, dynamic transmittance kinetics were evaluated at 650 nm (Fig. 4d), revealing a coloration time (t_c) and bleaching time (t_b) of 79.6 s and 25.2 s (Table S1†) for MVO, respectively. These switching speeds markedly outperform VO. The optical photos in the insets of Fig. 4d also show an apparent color change in MVO, while VO shows almost no change. As a critical EC metric, the CE values of MVO and VO are also correspondingly determined (Fig. S11†). CE is quantified as the optical density change (ΔOD) per unit charge density (ΔQ), defined by: $\text{CE} = \Delta\text{OD}/\Delta Q = \log(T_b/T_c)/\Delta Q$, where T_b and T_c represent transmittance in fully bleached and colored states at a specific wavelength, respectively, and ΔQ represents the amount of transferred charge. Linear fitting of optical density *versus* charge density during MVO coloration yields a CE value of $2.97 \text{ cm}^2 \text{ C}^{-1}$, significantly surpassing VO's $0.28 \text{ cm}^2 \text{ C}^{-1}$ (Fig. S11b†). The relatively low CE values might be due to the high capacity and multi-color characteristics of vanadates, resulting in an insignificant transmittance change when the same amount of charge is inserted/extracted. The faster switching time and larger optical modulation range as well as the larger CE may be attributed to the abundance of active sites provided by the MVO nanosheets as well as the faster redox kinetics of Zn^{2+} embedding/de-embedding.

To elucidate the electrochemical mechanism, *ex situ* XPS analysis was performed on MVO electrodes in the initial, reduced (0.2 V), and oxidized (2 V) states. The high-resolution XPS spectra of V 2p are shown in Fig. 4e–g, indicating the presence of V^{5+} , V^{4+} , and V^{3+} . Comparatively, when 0.2 V voltage is applied, MVO is reduced, and the peak area ratio of V^{4+} to V^{5+} gradually increases, while the proportion of V^{3+} basically remains unchanged. Reversely, when MVO is oxidized at 2 V, the proportion of V^{4+} gradually increases, with fewer V^{3+} remaining. It is thus speculated that the valence change between V^{3+} and V^{4+} is responsible for the redox reactions and the corresponding EC behavior in MVO.

Performance of electrochromic devices

Benefiting from the excellent electrochemical and EC properties of MVO electrodes, a ZECD was further assembled with

a MVO cathode, zinc foil as the anode, and 0.5 M ZnSO_4 aqueous electrolyte. As shown in Fig. 5a, the operation mechanism of the ZECD is the reversible Zn^{2+} (de)intercalation from/into MVO during charging/discharging. This phenomenon concurrently induces vanadium(v) valence change,⁴⁸ and thus color variations in the MVO-based ZECD.

CV and voltage-step cycling tests were conducted to evaluate the electrochemical reversibility of the ZECDs. Fig. 5b presents CV curves acquired at a scan rate of 20 mV s^{-1} within 0.2–2 V. Distinct redox peaks near 1.5 V (oxidation) and 0.8 V (reduction) correspond to redox reactions associated with vanadium valence changes, and the MVO-based ZECD demonstrates exceptional electrochemical reversibility. To evaluate the cycling stability of the MVO-based ZECD, we determined the CV curves (Fig. S12†) of the MVO-based ZECD for 100 cycles at a scan rate of 50 mV s^{-1} within 0.2–2 V. From Fig. S12,† it can be seen that during the process of 100 cycles, the degree of peak current decrease is not significant, which confirms that the ZECD based on MVO has excellent cycling stability. In contrast, VO counterparts (Fig. S13†) exhibit progressive peak attenuation and stability degradation in the first five cycles. The superior reversibility of MVO can likely be attributed to the Mg^{2+} intercalation-induced structural modification in V_2O_5 , which significantly enlarges the host lattice spacing. The expanded framework facilitates reversible Zn^{2+} intercalation kinetics, thereby enhancing the electrochemical stability of zinc-ion storage and improving long-term cycling durability. Meanwhile, it can also be seen from the digital photographs that the change in the valence state of V is accompanied by a distinct color change. Additionally, the MVO-based device shows obvious variations in transmittance (400–800 nm) spectra when MVO is in the initial, oxidized, and reduced states (Fig. 5c), with coloration/bleaching kinetics ($t_c = 76 \text{ s}$, $t_b = 33 \text{ s}$) similar to those of the individual MVO electrode. These consistent electrochemical responses and optical behaviors collectively validate the functional integrity and operational viability of the MVO-based ZECDs. Furthermore, the current responses in the MVO-based ZECDs demonstrate great stability over 500 cycles (Fig. 5e), obviously surpassing those of the VO-based ZECDs, confirming the outstanding cycling stability of the MVO-based ZECDs. Notably, it was observed that the current response exhibited significant variations during the first 100 cycles. We attribute this phenomenon primarily to two factors occurring during the initial cycling stages. First, Zn^{2+} intercalation/deintercalation induces irreversible structural changes within the VO lattice. Secondly, the inserted Zn ions, located at the “dead Zn^{2+} sites”, cannot be fully extracted from the VO lattice during the following charging process. These two points resulted in a decrease in the current response.^{28,56–58} This phenomenon is also consistent with the CV results measured previously. The electrochemical impedance spectroscopy (EIS) analysis of the ZECDs before and after cycling (Fig. 5f) further corroborates the performance advantages of MVO over VO. The VO-based ZECD experiences significant charge transfer resistance (R_{ct}) increases with cycling, while MVO maintains lower and more

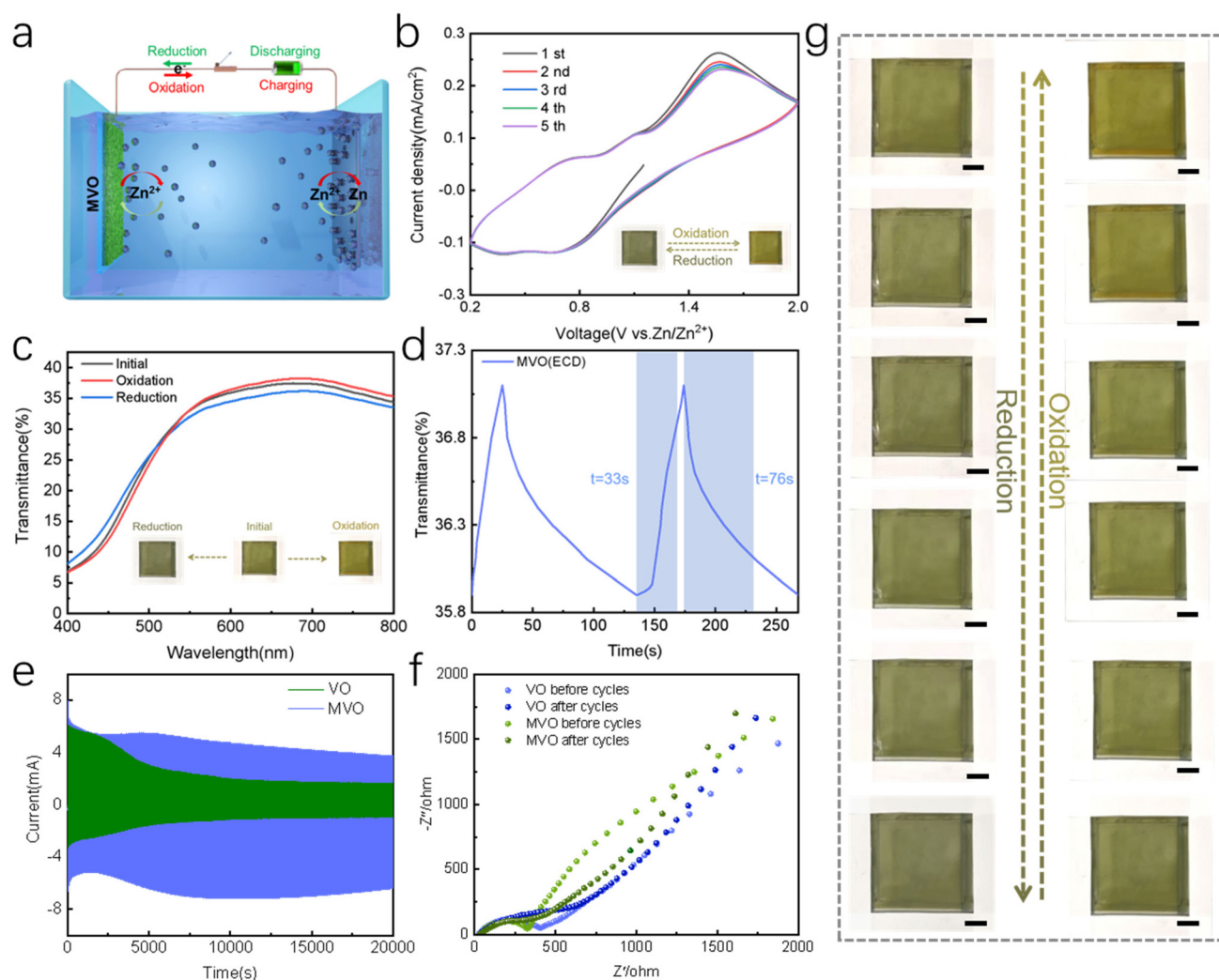


Fig. 5 (a) Schematic diagram of the ZECD working principle. (b) CV curves for the first 5 cycles of the MVO-based ZECD at 20 mV s^{-1} . Insets show the corresponding photographs of ZECDs in the oxidized and reduced states. (c) Transmission spectra and digital photographs of the MVO-based ZECD when MVO is in the initial state, oxidized state and reduced state. (d) *In situ* transmission response of the MVO-based ZECD at 650 nm at voltage steps of 0.2 V for 120 s and 2 V for 30 s . (e) Current change curves of ZECDs during 500 cycles at applied voltage steps of 0.2 V and 2 V for 20 s each. (f) Nyquist plots of VO and MVO-based ZECDs before and after cycling. (g) Color change process of MVO-based ZECDs ($5 \times 5 \text{ cm}^2$). Scale bar: 1 cm . ZECDs are reduced and oxidized at voltage steps of 0.2 V , 60 s and 2 V , 60 s , respectively. Each photograph was taken at a time interval of 10 s .

stable R_{ct} values throughout cycling. To demonstrate the dual EC-energy storage functionality, a full-cell ZECD ($5 \times 5 \text{ cm}$) was fabricated (Fig. 5g), showing an obvious reversible green-yellow color transition during charging and discharging, unambiguously verifying its bifunctional operation, promising for multifunctional ECDs.

Conclusion

In this study, magnesium-doped vanadium oxide (MVO) nanosheets were synthesized with good crystallinity using a simple hydrothermal method. The magnesium doping strategy can effectively expand the interlayer spacing of the host lattice and offer more active sites of vanadates while preserving the original layered structure, thus improving the cycling stability

and switching kinetics while delivering excellent energy storage and EC performance. Mechanistic studies reveal that Mg^{2+} intercalation within the V_2O_5 framework facilitates Zn^{2+} storage and intercalation/deintercalation kinetics. Compared to pristine VO, the MVO electrode exhibited a higher specific capacity of 57.6 mAh m^{-2} at 0.01 mA cm^{-2} , enhanced cycling stability, and improved rate capability, as well as accelerated switching kinetics (coloration time $t_c = 79.6 \text{ s}$, bleaching time $t_b = 25.2 \text{ s}$) and higher CE. Remarkably, the MVO-based ZECD retained robust current stability over 500 cycles, significantly outperforming its VO counterpart. The MVO-based ZECD ($5 \times 5 \text{ cm}^2$) also retained fast switching times ($t_c = 76 \text{ s}$, $t_b = 33 \text{ s}$) and obvious color changing behavior. These findings highlight the potential of Mg-doped vanadate architectures for developing high-performance ECDs with synergistically enhanced energy storage and optical modulation properties.

Author contributions

J. W. Chen and B. Xu supervised the study. M. J. Zhu provided assistance with characterization. C. F. Niu, G. L. Zhou and T. Z. He contributed to data analysis. All authors contributed to the general discussion.

Conflicts of interest

The authors declare no conflict of interest.

Data availability

The data supporting this article have been included as part of the ESI.†

Acknowledgements

This work was supported by the National Natural Science Foundation of China (No. 52202320), Fundamental Research Funds for the Central Universities (No. 862201013153), and Shandong Excellent Young Scientists Fund Program (Overseas) (2023HWYQ-060).

References

- 1 X. Yang, J. Zhang, S. Ren and Q. Ran, *J. Cleaner Prod.*, 2021, **287**, 125015.
- 2 S. H. Sutar, B. M. Babar, K. B. Pisal, A. I. Inamdar and S. H. Mujawar, *J. Energy Storage*, 2023, **73**, 109035.
- 3 W. F. Pickard, *Proc. IEEE*, 2014, **102**, 1094–1105.
- 4 G. Ren, H. Wang, C. Chen and J. Wang, *Sustainable Energy Technol. Assess.*, 2021, **44**, 100998.
- 5 H. Li and A. Y. Elezzabi, *Nanoscale Horiz.*, 2020, **5**, 691–695.
- 6 Z. Wang, X. Wang, S. Cong, F. Geng and Z. Zhao, *Mater. Sci. Eng., R*, 2020, **140**, 100524.
- 7 K. Gao, S. Ju, S. Li, S. Zhang, J. Liu, T. Yang, J. Lv, W. Yu and Z. Zhang, *ACS Nano*, 2023, **17**, 18359–18371.
- 8 J. Chen, A. L.-S. Eh, J.-H. Ciou and P. S. Lee, *Mater. Today Energy*, 2022, **27**, 101048.
- 9 Y. Wang, H. Jiang, R. Zheng, J. Pan, J. Niu, X. Zou and C. Jia, *J. Mater. Chem. A*, 2020, **8**, 12799–12809.
- 10 T. T. A. Nguyen, B. S. Soram, D. T. Tran, N. H. Kim and J. H. Lee, *Chem. Eng. J.*, 2023, **452**, 139555.
- 11 W. Wang, Z. Bai, B. Wang, X. Yang, J. Liu, H. Li, Y. Li, Q. Zhang, C. Hou, K. Li and H. Wang, *Small*, 2024, **20**, 2405152.
- 12 A. Kumar, J. Li, A. K. Inge and S. Ott, *ACS Nano*, 2023, **17**, 21595–21603.
- 13 J. Su, L. Chen, C. Xu, Y. Liu, L. Shen and Z. He, *J. Mater. Chem. A*, 2024, **12**, 29383–29401.
- 14 Z. Qi, T. Xiong, T. Chen, W. Shi, M. Zhang, Z. W. J. Ang, H. Fan, H. Xiao, W. S. V. Lee and J. Xue, *J. Alloys Compd.*, 2021, **870**, 159403.
- 15 J. Chen, B. Xu, Y. Zhang, W. Zhang, H. Wang, A. Y. Elezzabi, L. Liu, W. W. Yu and H. Li, *Appl. Phys. Rev.*, 2024, **11**, 011316.
- 16 B. Xu, J. Chen, Z. Ding, J. Hu, Y. Zhang, H. Li and H. Wang, *Small Sci.*, 2023, **3**, 2300025.
- 17 B. Wang, W. Zhang, F. Zhao, W. W. Yu, A. Y. Elezzabi, L. Liu and H. Li, *Nano Mater. Sci.*, 2023, **5**, 369–391.
- 18 H. Tang, F. Xiong, Y. Jiang, C. Pei, S. Tan, W. Yang, M. Li, Q. An and L. Mai, *Nano Energy*, 2019, **58**, 347–354.
- 19 Y. Huang, B. Wang, F. Chen, Y. Han, W. Zhang, X. Wu, R. Li, Q. Jiang, X. Jia and R. Zhang, *Adv. Opt. Mater.*, 2022, **10**, 2101783.
- 20 R. J. Gummow, G. Vamvounis, M. B. Kannan and Y. He, *Adv. Mater.*, 2018, **30**, 1801702.
- 21 Z. Li, Y. An, S. Dong, C. Chen, L. Wu, Y. Sun and X. Zhang, *Energy Storage Mater.*, 2020, **31**, 252–266.
- 22 B. Xu, J. Chen, P. Li, Y. Ouyang, Y. Ma, H. Wang and H. Li, *Nanoscale*, 2023, **15**, 19629–19637.
- 23 W. Li, C. Han, Q. Gu, S.-L. Chou, J.-Z. Wang, H.-K. Liu and S.-X. Dou, *Adv. Energy Mater.*, 2020, **10**, 2001852.
- 24 M. Wang, J. Zhang, L. Zhang, J. Li, W. Wang, Z. Yang, L. Zhang, Y. Wang, J. Chen, Y. Huang, D. Mitlin and X. Li, *ACS Appl. Mater. Interfaces*, 2020, **12**, 31564–31574.
- 25 B. Lee, H. R. Lee, H. Kim, K. Y. Chung, B. W. Cho and S. H. Oh, *Chem. Commun.*, 2015, **51**, 9265–9268.
- 26 Y. Zhang, A. Chen and J. Sun, *J. Energy Chem.*, 2021, **54**, 655–667.
- 27 G. Yoo, B.-R. Koo and G. H. An, *Chem. Eng. J.*, 2022, **434**, 134738.
- 28 P. He, G. Zhang, X. Liao, M. Yan, X. Xu, Q. An, J. Liu and L. Mai, *Adv. Energy Mater.*, 2018, **8**, 1702463.
- 29 H. Jiang, W. Gong, Y. Zhang, X. Liu, M. Waqar, J. Sun, Y. Liu, X. Dong, C. Meng, Z. Pan and J. Wang, *J. Energy Chem.*, 2022, **70**, 52–58.
- 30 M. A. Çarpan, O. Şentürk, S. R. Tokgöz, S. Sarsıcı, S. K. Akay and A. Peksöz, *Ceram. Int.*, 2024, **50**, 33111–33122.
- 31 S. Sarsıcı, S. R. Tokgöz, M. A. Çarpan, A. Olkun, S. K. Akay and A. Peksöz, *Surf. Interfaces*, 2024, **54**, 105269.
- 32 Z. Wang, P. Liang, R. Zhang, Z. Liu, W. Li, Z. Pan, H. Yang, X. Shen and J. Wang, *Appl. Surf. Sci.*, 2021, **562**, 150196.
- 33 T. Xiong, Z. G. Yu, H. Wu, Y. Du, Q. Xie, J. Chen, Y.-W. Zhang, S. J. Pennycook, W. S. V. Lee and J. Xue, *Adv. Energy Mater.*, 2019, **9**, 1803815.
- 34 Y. Zhang, Z. Li, B. Zhao, D. Xu, Z. Guo, J. Zhang and C. Gong, *ACS Sustainable Chem. Eng.*, 2025, **13**, 2553–2563.
- 35 M. Liao, J. Wang, L. Ye, H. Sun, Y. Wen, C. Wang, X. Sun, B. Wang and H. Peng, *Angew. Chem., Int. Ed.*, 2020, **59**, 2273–2278.
- 36 Y. Liu, Y. Sun, J. Zhang, X. Hao, M. Zhang, P. Wei, X. Zhao and K. Cai, *Nano Energy*, 2024, **120**, 109152.
- 37 W. Zhou, J. Chen, C. He, M. Chen, X. Xu, Q. Tian, J. Xu and C.-P. Wong, *Electrochim. Acta*, 2019, **321**, 134689.

- 38 Y. Yang, Y. Tang, G. Fang, L. Shan, J. Guo, W. Zhang, C. Wang, L. Wang, J. Zhou and S. Liang, *Energy Environ. Sci.*, 2018, **11**, 3157–3162.
- 39 S. Islam, M. H. Alfaruqi, D. Y. Putro, V. Soundharrajan, B. Sambandam, J. Jo, S. Park, S. Lee, V. Mathew and J. Kim, *J. Mater. Chem. A*, 2019, **7**, 20335–20347.
- 40 B. Sambandam, V. Soundharrajan, S. Kim, M. H. Alfaruqi, J. Jo, S. Kim, V. Mathew, Y.-k. Sun and J. Kim, *J. Mater. Chem. A*, 2018, **6**, 15530–15539.
- 41 Y. Zhao, C. Han, J. Yang, J. Su, X. Xu, S. Li, L. Xu, R. Fang, H. Jiang, X. Zou, B. Song, L. Mai and Q. Zhang, *Nano Lett.*, 2015, **15**, 2180–2185.
- 42 C. Xia, J. Guo, P. Li, X. Zhang and H. N. Alshareef, *Angew. Chem., Int. Ed.*, 2018, **57**, 3943–3948.
- 43 Z. Song, B. Wang, W. Zhang, Q. Zhu, A. Y. Elezzabi, L. Liu, W. W. Yu and H. Li, *Nano-Micro Lett.*, 2023, **15**, 229.
- 44 W. Zhang, H. Li, W. W. Yu and A. Y. Elezzabi, *Light: Sci. Appl.*, 2020, **9**, 121.
- 45 Y. Zhang, S. Cui, J. Zhang, W. Wei, Z. Yin, D. Chen, J. Zha and Q. Zhu, *Ionics*, 2025, **31**, 4739–4746.
- 46 Z. Song, B. Wang, W. Zhang, Q. Zhu, A. Y. Elezzabi, L. Liu, W. W. Yu and H. Li, *Nano-Micro Lett.*, 2023, **15**, 229.
- 47 M. Clites and E. Pomerantseva, *Energy Storage Mater.*, 2018, **11**, 30–37.
- 48 F. Ming, H. Liang, Y. Lei, S. Kandambeth, M. Eddaoudi and H. N. Alshareef, *ACS Energy Lett.*, 2018, **3**, 2602–2609.
- 49 J. Yang, X. Wang, J. Wang, X. Dong, L. Zhu, D. Hou, W. Zeng, J. Wang and F. Pan, *Appl. Surf. Sci.*, 2021, **569**, 150983.
- 50 X. Wang, Z. Zhang, S. Xiong, F. Tian, Z. Feng, Y. Jia, J. Feng and B. Xi, *Small*, 2021, **17**, 2100318.
- 51 D. Kundu, B. D. Adams, V. Duffort, S. H. Vajargah and L. F. Nazar, *Nat. Energy*, 2016, **1**, 16119.
- 52 R. Verrelli, A. P. Black, C. Pattanathummasid, D. S. Tchitchekova, A. Ponrouch, J. Oró-Solé, C. Frontera, F. Bardé, P. Rozier and M. R. Palacín, *J. Power Sources*, 2018, **407**, 162–172.
- 53 X. Guo, G. Fang, W. Zhang, J. Zhou, L. Shan, L. Wang, C. Wang, T. Lin, Y. Tang and S. Liang, *Adv. Energy Mater.*, 2018, **8**, 1801819.
- 54 R. Shanthappa, A. K. Kakarla, H. Bandi, W. A. Syed and J. S. Yu, *J. Magnesium Alloys*, 2025, **13**, 1660–1670.
- 55 L.-H. Hu, K.-S. Hsiao and C.-T. Wang, *Electrochim. Acta*, 2025, **524**, 146055.
- 56 J.-K. Kim, B. Senthilkumar, S. H. Sahgong, J.-H. Kim, M. Chi and Y. Kim, *ACS Appl. Mater. Interfaces*, 2015, **7**, 7025–7032.
- 57 L. Mai, L. Xu, C. Han, X. Xu, Y. Luo, S. Zhao and Y. Zhao, *Nano Lett.*, 2010, **10**, 4750–4755.
- 58 F. Zhao, B. Wang, B. Huang, W. Zhang, J. Chen, L. Liu, H. Wang, A. Y. Elezzabi, P. S. Lee, D. J. Milliron, W. W. Yu and H. Li, *Nat. Rev. Clean Technol.*, 2025, **1**, 396–412.